Supplementary Material for: Quasi-cubic model for metal halide perovskite nanocrystals

Peter C. Sercel[1,a)], John L. Lyons[2], Noam Bernstein[2], and Alexander L. Efros[2]

[1] *Department of Applied Physics and Materials Science, California Institute of Technology, Pasadena, California 91125, USA; Electronic mail: psercel@caltech.edu*

[a)] *Also at Center for Hybrid Organic Inorganic Semiconductors for Energy, 15013 Denver West Parkway, Golden, CO 80401, USA*

[2] *Center for Computational Materials Science, U. S. Naval Research Laboratory, Washington DC 20375 USA*

CONTENTS

1. COUPLED BAND MODEL FOR QUANTUM SIZE LEVELS IN SPHERICAL NANOCRYSTALS

In cubic phase metal halide perovskites (MHPs), the conduction and valence band edges are located at the R-point of the first Brilluoin zone[1], for which the point symmetry group is O_h[2, 11]. We first develop a model for the confined conduction and valence band levels of a

MHP nanocrystal in terms of the multiband $\boldsymbol{k}\cdot\boldsymbol{P}$ theory developed for spherical nanocrystals [4, 5].

In the MHPs, the band edge states of the lowest conduction band transforms as a state with p orbital symmetry with total angular momentum $J = 1/2$: The conduction band edge states $|1/2, \pm 1/2\rangle_c$, given by [2],

$$|1/2, 1/2\rangle_c = \frac{-1}{\sqrt{3}} \left[(|X\rangle + i|Y\rangle) \left| \downarrow \right\rangle + |Z\rangle \left| \uparrow \right\rangle \right]$$
$$|1/2, -1/2\rangle_c = \frac{1}{\sqrt{3}} \left[- (|X\rangle - i|Y\rangle) \left| \uparrow \right\rangle + |Z\rangle \left| \downarrow \right\rangle \right]. \quad (1)$$

The valence band edge states can be represented as the $J = 1/2$ states with s orbital symmetry, which we write $|1/2, \pm 1/2\rangle_v$, given by [2]:

$$|1/2, 1/2\rangle_v = |S\rangle \left| \uparrow \right\rangle, \quad |1/2, -1/2\rangle_v = |S\rangle \left| \downarrow \right\rangle, \quad (2)$$

In these expressions the spinor functions $|\uparrow\rangle$ and $|\downarrow\rangle$ are the eigenfunctions of the electron spin projection operator $s_z = \pm 1/2$.

Given the point symmetry O_h we can approximate the conduction and valence band eigenstate in spherical NCs as eigenstates of total angular momentum $\boldsymbol{F}$ and its projection F_z,[4]. It is therefore convenient to represent these states in a total angular momentum basis written as follows:

$$|F, F_z\rangle = \sum_L R_{L,F}(r) \, |F, F_z; J, L\rangle. \quad (3)$$

Here, the $R_{L,F}$ are radial envelope functions and the angular basis functions $|F, F_z; J, L\rangle$ are constructed as [4],

$$|F, F_z; J, L\rangle = \sum_{J_z=-J}^{J} \sum_{L_z=-L}^{L} \langle J, J_z; L, L_z | F, F_z \rangle \;\; |J, J_z\rangle \;\; |L, L_z\rangle. \quad (4)$$

The first term in the sum above is a Clebsch-Gordan coefficient; the states $|J, J_z\rangle$ are band edge Bloch functions with $J = 1/2$, and $|L, L_z\rangle$ are envelope functions which have coordinate representations given by spherical harmonics.

Using this basis we express the effective mass Hamiltonian for flat band conditions in a free spherical wave basis of eigenstates of total angular momentum. The appropriate basis functions inside the NC are the spherical waves which are regular at the origin[4]:

$$|k, F, F_z; J, L\rangle = \sqrt{\frac{2}{\pi}} i^L j_L(kr) |F, F_z; J, L\rangle \quad (5)$$

where $j_L(kr)$ is a spherical Bessel function with wavenumber k. In this basis the Hamiltonian is block diagonal in F, F_z and parity. [4] For bound states, outside the NC the appropriate basis functions take the form of spherical Hankel functions of the first kind, which we denote at h_L, which decay with increasing radius for imaginary wavenumber $k = i\lambda$[4]:

$$|k, F, F_z; J, L\rangle = \sqrt{\frac{2}{\pi}} i^L h_L(kr)|F, F_z; J, L\rangle \tag{6}$$

A. Kang Wise model

A four band model for the coupled conduction-valence band system is given in a Bloch plane-wave basis in Ref [2]. This Hamiltonian is equivalent to the one developed in the spherical approximation for lead chalcogenide NCs by Kang and Wise in Ref. [5]. Applying a unitary basis transformation, this Hamiltonian can be rewritten in the spherical wave basis, Eq. 4 [4]; in this form the Hamiltonian is block-diagonal in total angular momentum F, F_z and parity. We consider only the lowest energy conduction and valence band states, which correspond to total angular momentum $F = 1/2$. We use the notation $|\mathrm{J}, \mathrm{L}\rangle$ to denote our basis with the quantum numbers $\mathrm{F} = 1/2$ and $\mathrm{F_z} = \pm 1/2$ in $|\mathrm{F}, \mathrm{F_z}; \mathrm{J}, \mathrm{L}\rangle$ understood and therefore omitted. In this basis the Hamiltonian within the subspace of the lowest angular momentum $F = 1/2$ states for odd (even) parity is given by,

$$\mathbf{H}^{0(1)}_{1/2,\pm 1/2} = \begin{array}{c} \\ |1/2, 0(1)\rangle_c \\ |1/2, 1(0)\rangle_v \end{array} \begin{array}{c} \begin{array}{cc} |1/2, 0(1)\rangle_c & |1/2, 1(0)\rangle_v \end{array} \\ \begin{pmatrix} E_c + \gamma_c \frac{\hbar^2 k^2}{2m_0} & -i\frac{\hbar}{m_0}\sqrt{\frac{1}{3}}Pk \\ i\frac{\hbar}{m_0}\sqrt{\frac{1}{3}}Pk & E_v - \gamma_v \frac{\hbar^2 k^2}{2m_0} \end{pmatrix} \end{array}, \tag{7}$$

where γ_e and γ_h are dimensionless parameters that represent the contribution of remote bands to the effective mass of the electrons and holes, respectively, m_0 is the free electron mass and the matrix element $P = -i\langle S|\hat{P}|Z\rangle$ is the Kane momentum matrix element, related to the Kane energy by $E_p = 2|P|^2/m_0$. In all the expressions m_o denotes the free electron mass. We diagonalize this matrix to obtain the nonparabolic two-band dispersion relation

$$(A_c - E)(A_v - E) = \frac{1}{3}\frac{\hbar^2}{m_0^2}P^2k^2 = \frac{E_p}{3}\frac{\hbar^2}{2m_0}k^2 \tag{8}$$

In this expression the terms $A_{c(v)}$ are defined by,

$$A_c(k) = E_c + \gamma_c \frac{\hbar^2 k^2}{2m_0}, \quad A_v(k) = E_v - \gamma_v \frac{\hbar^2 k^2}{2m_0}, \tag{9}$$

Because Eq 8 is quartic in k, there are therefore two solutions for k^2 for a given energy. We note that one of the two solutions corresponds to a pure imaginary solution for all energies; we denote the solutions as $k_1^2 = k^2$ (real solution for $E > E_c$ or $E < E_v$) and $k_2^2 = -\lambda^2$ (imaginary solution). In this case the QD eigenstates are found by superposing the two bulk radial wave states associated with wavenumbers $k_{1,2}^2$ that are regular at the origin. For the conduction states with $F = 1/2$, the general form can thus be written [4],

$$\psi(r) = A \begin{pmatrix} j_l(kr) \\ \Theta_c(E,k)\ j_{|1-l|}(kr) \end{pmatrix} + B \begin{pmatrix} j_l(i\lambda r) \\ \Theta_c(E,i\lambda)\ j_{|1-l|}(i\lambda r) \end{pmatrix} \tag{10}$$

where using $l = 0$ corresponds to the S-like ground state while $l = 1$ corresponds to the excited P-like states. The functions $\Theta_c(E,k)$ involved in the bulk radial waves are given by,

$$\Theta_c(E,K) = -i\frac{\hbar}{m_0}\sqrt{\frac{1}{3}}Pk\frac{1}{A_v(k) - E} \tag{11}$$

It is convenient to express the Kane matrix element P in terms of the Kane energy $E_p = 2P^2/m_o$:

$$P = \sqrt{\frac{m_0 E_p}{2}} \tag{12}$$

Using this we can re-write the Θ function as,

$$\Theta_c(E,k) = -i\sqrt{\frac{1}{3}}\sqrt{\frac{\hbar^2 E_p}{2m_0}}\frac{k}{A_v(k) - E} \tag{13}$$

The requirement that the wavefunction vanish at the NC surface $r = R$ leads to the dispersion relation [5],

$$\frac{j_l(kR)\ j_{|1-l|}(i\lambda R)}{j_{|1-l|}(kR)\ j_l(i\lambda R)} = \frac{\Theta_c(E,k)}{\Theta_c(E,i\lambda)} = -i\frac{k}{\lambda}\frac{(A_v(i\lambda) - E)}{(A_v(k) - E)} \tag{14}$$

Equations (8), and (14) form a system of three equations in the three unknowns, E, k, and λ. In the limit that the parameters $\gamma_c \to 0$ and $\gamma_v =\!\!\to 0$, the parameter λ goes to the limit,

$$\lambda \to \frac{1}{\gamma_{c,v}}\sqrt{\frac{2m_0}{\hbar^2}\frac{E_p}{3}} \to \infty \tag{15}$$

In this limit,

$$\lim_{\lambda\to\infty}\frac{j_1(i\lambda R)}{j_0(i\lambda R)} = +i \tag{16}$$

Additionally, in this limit,

$$\lim_{\lambda\to\infty}\frac{\lambda}{A_v(\lambda)-E}=\frac{2m_0}{\hbar^2}\frac{1}{\gamma_{c,v}\lambda}=\sqrt{\frac{2m_0}{\hbar^2}}\sqrt{\frac{3}{E_p}} \tag{17}$$

Thus, the eigenvalues for the case $\gamma_{c,v}\to\infty$ are found by solving the equation,

$$\frac{j_l(kR)}{j_{|1-l|}(kR)}=(-1)^{l+1}\sqrt{\frac{\hbar^2}{2m_0}}\sqrt{\frac{E_p}{3}}\frac{k}{(E_v-E)} \tag{18}$$

A parallel analysis for the valence states can be made using,

$$\psi(r)=A\begin{pmatrix}\Theta_v(E,k)\ j_{|1-l|}(kr)\\ j_l(kr)\end{pmatrix}+B\begin{pmatrix}\Theta_v(E,i\lambda)\ j_{|1-l|}(i\lambda r)\\ j_l(i\lambda r)\end{pmatrix} \tag{19}$$

where using $l=0$ corresponds to the S-like ground valence band quantum size level state while again $l=1$ corresponds to the excited P-like envelope states. Here,

$$\Theta_v(E,k)=+i\sqrt{\frac{1}{3}}\sqrt{\frac{\hbar^2E_p}{2m_0}}\frac{k}{A_c(k)-E} \tag{20}$$

This leads to the eigenvalue equation for those states as,

$$\frac{j_l(kR)\ j_{|1-l|}(i\lambda R)}{j_{|1-l|}(kR)\ j_l(i\lambda R)}=\frac{\Theta_v(E,k)}{\Theta_v(E,i\lambda)}=-i\frac{k}{\lambda}\frac{(A_c(i\lambda)-E)}{(A_c(k)-E)} \tag{21}$$

When $\gamma_c\to 0$ and $\gamma_v=\!\!\to 0$, this has the limit,

$$\frac{j_l(kR)}{j_{|1-l|}(kR)}=(-1)^{l+2}\sqrt{\frac{\hbar^2}{2m_0}}\sqrt{\frac{E_p}{3}}\frac{k}{E_c-E} \tag{22}$$

The sign change relative to Eq. 18 follows since,

$$\frac{\lambda}{A_c(i\lambda)-E}=\frac{\lambda}{E_c-E-(\hbar^2/2m_0)\gamma_v\lambda^2} \tag{23}$$

and since as $\gamma_v\to 0$, $\lambda\to(1/\gamma_v)\sqrt{(2m_0/\hbar^2)E_p/3}$, it follows that,

$$\lim_{\gamma_v\to 0}\frac{\lambda}{A_c(i\lambda)-E}=-\sqrt{\frac{3}{E_p}\frac{2m_0}{\hbar^2}} \tag{24}$$

It is seen that the confinement energies of the valence and conduction band states relative to their respective band edges are equal.

B. Kane model

The four band model for the coupled conduction-valence band system given in Ref [2] in general contains terms on the diagonal that are quadratic in the wave-vector, and therefore can give rise to non-physical "wing-band" states of imaginary wave-vector for non-zero γ_c, γ_v. As a check we therefore implement a Kane-type model [6] inwhich these quadratic terms are neglected from the outset and the NC is treated as a heterostructure with finite band offset [4]. To check the result previously derived we will then take the limit of the resulting expressions in the limit of infinite band offset /barrier height.

We use the notation $|\mathrm{J}, \mathrm{L}\rangle$ to denote our basis with the quantum numbers $\mathrm{F} = 1/2$ and $\mathrm{F_z} = \pm 1/2$ in $|\mathrm{F}, \mathrm{F_z}; \mathrm{J}, \mathrm{L}\rangle$ for the lowest energy states understood and therefore omitted. In this basis the Kane Hamiltonian within the subspace of the lowest angular momentum states for odd (even) parity is given by,

$$\mathbf{H}^{0(1)}_{1/2,\pm 1/2} = \begin{array}{c} \\ |1/2,0(1)\rangle_c \\ |1/2,1(0)\rangle_v \end{array} \begin{array}{c} \begin{array}{cc} |1/2,0(1)\rangle_c & |1/2,1(0)\rangle_v \end{array} \\ \begin{pmatrix} E_c & -i\frac{\hbar}{m_0}\sqrt{\frac{1}{3}}Pk \\ i\frac{\hbar}{m_0}\sqrt{\frac{1}{3}}Pk & E_v \end{pmatrix} \end{array} \tag{25}$$

We diagonalize this matrix to obtain the nonparabolic two-band dispersion relation

$$(E_c - E)(E_v - E) = \frac{1}{3}\frac{\hbar^2}{m_0^2}P^2k^2 = \frac{E_p}{3}\frac{\hbar^2}{2m_0}k^2 \tag{26}$$

where we used the definition of the Kane energy, $E_p = 2P^2/m_0$.

We illustrate the solution for the nanocrystal for the case of conduction band states. The eigenfunctions for the conduction band states with $F = 1/2$ are found as follows: We form the Hamiltonian peice-wise with bandstructure constants $\mathrm{E_c^I}$, $\mathrm{E_v^I}$ within the nanocrystal and $\mathrm{E_c^O}$, $\mathrm{E_v^O}$ exterior to it. Eigenvectors of the 2×2 Hamiltonian are computed interior and exterior to the quantum dot. We require that the wavefunction be regular at the origin. The boundary condition that the wavefunction be continuous across the interface is applied to arrive at a relation between spherical wave numbers inside and outside. This condition is combined with the energy dispersion relations to determine the eigenvalues of the quantum dot. The energy dispersion relations follow from Eq.(26) and are given by the expressions

$$\begin{aligned} (E_c^I - E)(E_v^I - E) &= \frac{E_p}{3}\frac{\hbar^2}{2m_0}k^2 \\ (E_c^O - E)(E_v^O - E) &= -\frac{E_p}{3}\frac{\hbar^2}{2m_0}\lambda^2, \end{aligned} \tag{27}$$

where the exterior spherical wavenumber has been taken as $i\lambda$ in anticipation of solving for bound energy eigenstates. Eigenvectors resulting from the diagonalization process have the same general form as described above. For the conduction band states we form:

$$|\psi_E\rangle = A \ \{|1/2, l\rangle + \Theta_c(E,k) \ |3/2, |1-l|\rangle \ \} \tag{28}$$

where $l = 0, 1$ depending on the parity of the conduction band envelope and where "A" is a constant to be determined by matching boundary conditions and applying normalization. The function Θ_c is,

$$\Theta_c(E,k) = -i\frac{\hbar}{m_0}\sqrt{\frac{1}{3}}Pk\frac{1}{(E_v - E)} \tag{29}$$

The angular and Bloch space elements of Eq.(28) are assumed to be the same inside and outside the dot, so this vector is projected onto only the envelope space radial coordinate representation. This results in a 2-dimensional column vector representation for the quantum dot state inside and outside the dot given by,

$$\psi^{in}(r) = A\begin{pmatrix} j_l(k_{in}r) \\ \Theta_c(E,k)\ j_{|1-l|}(k_{in}r)\end{pmatrix}, \quad \psi^{out}(r) = B\begin{pmatrix} h_l(k_{out}r) \\ \Theta_c(E,i\lambda)\ h_{|1-l|}(k_{out}r)\end{pmatrix}, \tag{30}$$

Note that outside the quantum dot, only the spherical Hankel function of imaginary argument which decays for large r is retained. Applying continuity of the resulting envelope states at the boundary of the quantum dot and $r = R$ leads to the following condition:

$$\frac{j_l(kR)\ h_{|1-l|}(i\lambda R)}{j_{|1-l|}(kR)\ h_l(i\lambda R)} = \frac{\Theta_c(E,k)}{\Theta_c(E,i\lambda)} = \frac{k}{i\lambda}\frac{(E_v^o - E)}{(E_v^{in} - E)} \tag{31}$$

which is very similar, but not identical, to what we had obtained in the Kang-Wise solution. Equations (27), and (32) form a system of three equations in the three unknowns, E, k, and λ. In the limit as the barrier heights goes to ∞, $E_v^o \to -E_B \to -\infty$ and $E_c^o \to +E_B \to +\infty$ so that, using Eq 27, we find

$$\frac{\lambda}{E_v - E} \to -\sqrt{\frac{3}{E_p}\frac{2m_0}{\hbar^2}}$$

In addition, in this case, $\lambda \to \infty$ so that,

$$\frac{h_1(i\lambda R)}{h_0(i\lambda R)} \to -i$$

Thus, the eigenvalues are found by solving the equation,

$$\frac{j_l(kR)}{j_{|1-l|}(kR)} = (-1)^{l+1}\sqrt{\frac{E_p}{3}\frac{\hbar^2}{2m_0}}\frac{k}{(E_v^{in} - E)} \tag{32}$$

This is exactly the same equation as produced in the Kang Wise model in the limit that $\gamma_c = \gamma_v \to 0$.

2. QUASI-CUBIC MODEL FOR BLOCH FUNCTIONS FOR TETRAGONAL AND ORTHORHOMBIC LATTICE SYMMETRY

We begin our analysis of the band edge Bloch functions with cubic phase perovskite, point group O_h. As previously noted, the band edges in the cubic phase are located at the R-point of the first Brillouin zone [1]. Since we will be considering the electronic structure of the orthorhombic phase we are free to visualize the electronic structure in a non-primitive supercell coincident with the orthorhombic primitive cell, that is, instead of referencing the primitive cubic cell of lattice constant a_0 aligned to the cubic symmetry axes, we reference a non-primitive cell spanned by vectors $\boldsymbol{a}$, $\boldsymbol{b}$, $\boldsymbol{c}$ of dimensions $\sqrt{2}a_0 : \sqrt{2}a_0 : 2a_0$ where the vectors $\boldsymbol{a}$, and $\boldsymbol{b}$ are rotated by 45^o to the cubic phase $\boldsymbol{x}, \boldsymbol{y}$ axes while the vector $\boldsymbol{c}$ is aligned to the cubic phase $\boldsymbol{z}$ axis and twice the length of the primitive vector. With reference to this non-primitive cell, the conduction and valence band edges are mapped onto the Γ point, that is, the center of the first Brillouin zone.

It is conceptually simplest to start the analysis considering the electronic structure neglecting spin-orbit coupling. In this case the band edge Bloch functions for the valence band are given by,

$$u^v = S \tag{33}$$

while the conduction band Bloch functions are given by

$$u^c_x = X\,, \quad u^c_y = Y\,, \quad u^c_z = Z\,. \tag{34}$$

In the equations above, S and X, Y, Z are the orbital Bloch functions for the s-type and p-type band edge symmetry, respectively. In this basis we consider the effect of the distortion of the unit cell carrying the structure from the cubic phase to the tetragonal or orthorhombic phase. The effect of these distortions is to change the lattice constants with respect to the cubic phase. We can parameterize the departure from the cubic phase lattice constants in terms of a strain whose principle axes coincide with the orthorhombic cell and model the effect on the conduction band edge states using a deformation potential model. As shown in the main text, the strain deformation Hamiltonian is constructed using the theory of invariants as,

$$\tilde{H}_d = U_d \left(e_{xx} L_x^2 + e_{yy} L_y^2 + e_{zz} L_z^2 - 2/3(e_{xx} + e_{yy} + e_{zz})\mathbb{I} \right) \tag{35}$$

where U_d is a deformation potential, e_{ii} are the components of the strain tensor with i running over x, y, z, taken parallel to the orthorhombic cell edges; while $L_{x,y,z}$ are the matrixes

representing the x, y and z projections of angular momentum $l = 1$. Together with $\mathbb{I}$, the 3x3 unit matrix, the $L_{x,y,z}$ serve as base matrices for the deformation potential Hamiltonian for the P-like conduction band with no spin orbit coupling. Here we are only interested in the splitting caused within the conduction band manifold and have separated out the volume dilatation term. Following the main text, we introduce the tetragonal, δ, and orthorhombic, ζ crystal field parameters as follows:

$$\delta \equiv U_d \left(\epsilon_{zz} - \frac{\epsilon_{xx} + \epsilon_{yy}}{2} \right) \ , \ \zeta \equiv U_d \frac{\epsilon_{xx} - \epsilon_{yy}}{2} \ . \tag{36}$$

We next add spin and spin-orbit coupling into the analysis. The spin-orbit coupling can be written as:

$$\hat{H}_{SO} = \frac{2}{3} \Delta_{so} \boldsymbol{L} \cdot \boldsymbol{S} \tag{37}$$

where $\boldsymbol{L}$ is the orbital angular momentum and $\boldsymbol{S}$ is the spin. In the absence of any deformation from cubic symmetry, the Bloch functions which diagonalize the SO interaction can be represented as the eigenstates of total angular momentum $\boldsymbol{J} = \boldsymbol{L} + \boldsymbol{S}$. We therefore change basis to a basis of total angular momentum states. For the valence band edge, these are the even parity states of angular momentum $J = 1/2$, which we write $u^v_{1/2,\pm 1/2}$, given by [2]:

$$u^v_{1/2,1/2} = S \uparrow, \quad u^v_{1/2,-1/2} = S \downarrow, \tag{38}$$

where the spinor functions $\uparrow$ and $\downarrow$ are the eigenfunctions of the electron spin projection operator $s_z = \pm 1/2$. The spin orbit interaction splits the conduction band into lower, band edge, states with angular momentum $J = 1/2$, and upper states with $J = 3/2$. The conduction band edge Bloch functions $u^c_{1/2,\pm 1/2}$ are given by [2],

$$u_{1/2,1/2} = \frac{-1}{\sqrt{3}} \left[(X + iY) \downarrow + Z \uparrow \right] , \qquad u_{1/2,-1/2} = \frac{1}{\sqrt{3}} \left[- (X - iY) \uparrow + Z \downarrow \right] . \tag{39}$$

while for the upper states with $J = 3/2$ the Bloch functions, $u_{3/2,\mu}$ ($\mu = \pm 3/2, \pm 1/2$) are,

$$\begin{aligned} u_{3/2,3/2} &= -\frac{1}{\sqrt{2}} (X + iY) \uparrow , \qquad u_{3/2,-3/2} = \frac{1}{\sqrt{2}} (X - iY) \downarrow , \\ u_{3/2,1/2} &= \frac{1}{\sqrt{6}} \left[- (X + iY) \downarrow + 2Z \uparrow \right] , \qquad u_{3/2,-1/2} = \frac{1}{\sqrt{6}} \left[(X - iY) \uparrow + 2Z \downarrow \right] . \end{aligned} \tag{40}$$

In this basis, taken in the order,

$$|3/2, 3/2\rangle, \ |3/2, 1/2\rangle, \ |3/2, -1/2\rangle, \ |3/2, 13/2\rangle, \ |1/2, 1/2\rangle, \ |1/2, -1/2\rangle,$$

the conduction band Hamiltonian $\hat{H} = \hat{H}_{SO} + \hat{H}_d$ is given by,

$$\hat{H}(\delta,\zeta) = \begin{pmatrix} \frac{1}{3}\Delta_{SO} + \frac{\delta}{3} & 0 & \frac{\zeta}{\sqrt{3}} & 0 & 0 & -\sqrt{\frac{2}{3}}\zeta \\ 0 & \frac{1}{3}\Delta_{SO} - \frac{\delta}{3} & 0 & \frac{\zeta}{\sqrt{3}} & \frac{\sqrt{2}\delta}{3} & 0 \\ \frac{\zeta}{\sqrt{3}} & 0 & \frac{1}{3}\Delta_{SO} - \frac{\delta}{3} & 0 & 0 & -\frac{\sqrt{2}\delta}{3} \\ 0 & \frac{\zeta}{\sqrt{3}} & 0 & \frac{1}{3}\Delta_{SO} + \frac{\delta}{3} & \sqrt{\frac{2}{3}}\zeta & 0 \\ 0 & \frac{\sqrt{2}\delta}{3} & 0 & \sqrt{\frac{2}{3}}\zeta & -\frac{2}{3}\Delta_{SO} & 0 \\ -\sqrt{\frac{2}{3}}\zeta & 0 & -\frac{\sqrt{2}\delta}{3} & 0 & 0 & -\frac{2}{3}\Delta_{SO} \end{pmatrix} \tag{41}$$

Let us now consider specific symmetries.

A. Tetragonal distortion

For the lattice structure with tetragonal symmetry, the crystal field parameter $\zeta = 0$ and the conduction band Hamiltonian $\tilde{H}$ assumes the simpler form,

$$\hat{H}(\delta,0) = \begin{pmatrix} \frac{\delta}{3} + \frac{1}{3}\Delta_{SO} & 0 & 0 & 0 & 0 & 0 \\ 0 & \frac{1}{3}\Delta_{SO} - \frac{\delta}{3} & 0 & 0 & \frac{\sqrt{2}\delta}{3} & 0 \\ 0 & 0 & \frac{1}{3}\Delta_{SO} - \frac{\delta}{3} & 0 & 0 & -\frac{\sqrt{2}\delta}{3} \\ 0 & 0 & 0 & \frac{\delta}{3} + \frac{1}{3}\Delta_{SO} & 0 & 0 \\ 0 & \frac{\sqrt{2}\delta}{3} & 0 & 0 & -\frac{2}{3}\Delta_{SO} & 0 \\ 0 & 0 & -\frac{\sqrt{2}\delta}{3} & 0 & 0 & -\frac{2}{3}\Delta_{SO} \end{pmatrix} \tag{42}$$

This Hamiltonian can be diagonalized giving the following energies: The upper 4-fold degenerate conduction band splits into two 2-fold degenerate bands which we label, in analogy to the valence bands in III-V semiconductors, as heavy-electrons (he) with $J = 3/2$, $J_z = \pm 3/2$, and light-electrons (le) with $J = 3/2$, $J_z = \pm 1/2$, while the lower spin-orbit split off band has $J = 1/2$, $J_z = \pm 1/2$, and is labeled c for the conduction band. The energies of these bands are,[7, 9, 10],

$$\begin{aligned} E_{le} &= -\frac{\Delta_{so}+\delta}{6} + \frac{1}{2}\sqrt{\Delta_{so}^2 - \frac{2}{3}\Delta_{so}\,\delta + \delta^2}; \qquad (J_z = \pm\frac{1}{2}) \\ E_{he} &= \frac{\Delta_{so}+\delta}{3}; \qquad (J_z = \pm\frac{3}{2}) \\ E_{c} &= -\frac{\Delta_{so}+\delta}{6} - \frac{1}{2}\sqrt{\Delta_{so}^2 - \frac{2}{3}\Delta_{so}\,\delta + \delta^2}; \qquad (J_z = \pm\frac{1}{2}). \end{aligned} \tag{43}$$

The corresponding eigenstates, which can be represented as eigenstates of the projection of total angular momentum along the c-axis, taken to be along z are written for the upper bands as:

$$u^{tet}_{le,1/2} = -\sin\theta\frac{(X+iY)}{\sqrt{2}}\downarrow + \cos\theta Z\uparrow, \qquad u^{tet}_{le,-1/2} = \sin\theta\frac{(X-iY)}{\sqrt{2}}\uparrow + \cos\theta Z\downarrow,$$
$$u^{tet}_{he,3/2} = -\frac{1}{\sqrt{2}}(X+iY)\uparrow, \qquad u^{tet}_{he,-3/2} = \frac{1}{\sqrt{2}}(X-iY)\downarrow \tag{44}$$

while the lowest conduction band has eigenstates,

$$u^{tet}_{c,1/2} = -\sin\theta Z\uparrow - \cos\theta\frac{X+iY}{\sqrt{2}}\downarrow$$
$$u^{tet}_{c,-1/2} = -\cos\theta\frac{X-iY}{\sqrt{2}}\uparrow + \sin\theta Z\downarrow \tag{45}$$

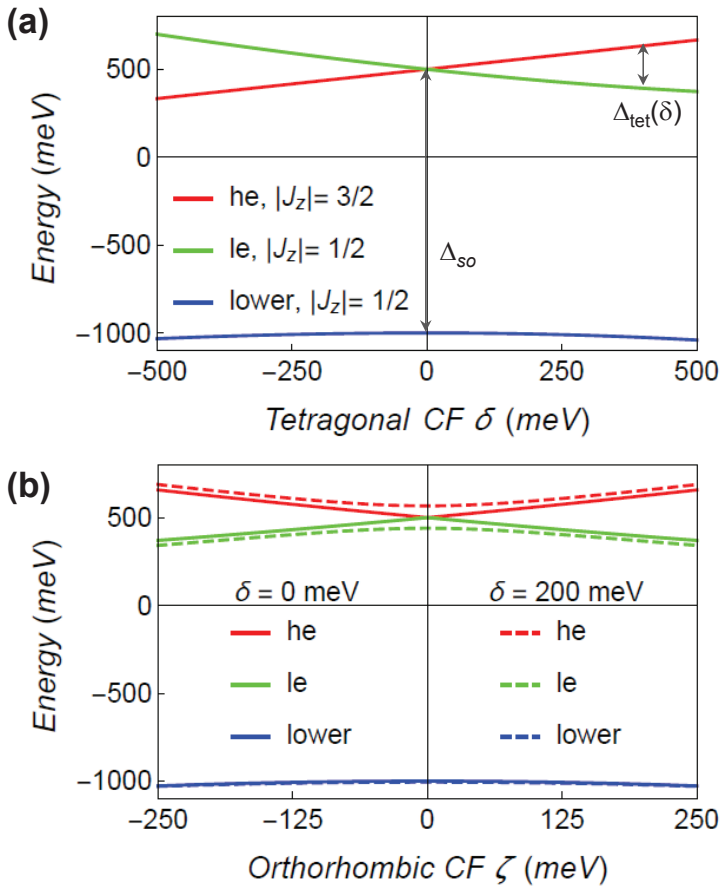

FIG. 1. Band edge/zone center conduction band energies plotted versus tetragonal crystal field δ, panel (a); and versus orthorhombic crystal field, ζ, in panel (b). Panel (a) is calculated using Eq. 43. In the figure the spin orbit splitting Δ_{SO} is taken as 1.5 eV and is labelled in the panel; it is the difference in energy between the upper $J = 3/2$ and the lower $J = 1/2$ conduction bands at zero distortion. The band energies are plotted relative to the energy centroid of the 6 conduction bands. One can see the tetragonal splitting $\Delta_{tet}(\delta)$ is described in Eq. 47, which is the splitting between the "he" $J_z = \pm 3/2$ bands and "le" $J_z = \pm 1/2$ bands. Panel (b) shows the split band edge energies plotted versus orthorhombic crystal field ζ. Calculations were conducted for tetragonal crystal fields $\delta = 0$ and $\delta = 200$ meV shown by solid and dashed lines, respectively.

In these expressions the angle θ is given by[8, 9],

$$\tan 2\theta = \frac{2\sqrt{2}\Delta_{SO}}{\Delta_{SO} - 3\delta} , \qquad (0 \le \theta \le \frac{\pi}{2}) . \tag{46}$$

This follows straightforwardly from the identity,

$$\tan 2\theta = \frac{2\tan\theta}{1-\tan^2\theta}$$

using,

$$\tan\theta = \frac{3\delta - \Delta_{so} + 3\sqrt{\Delta_{so}^2 - \frac{2}{3}\Delta_{so}\,\delta + \delta^2}}{2\sqrt{2}\Delta_{so}}\ .$$

Within this model, the tetragonal crystal field, δ, splits the $J = 3/2$ conduction band states by an amount,[7, 9, 10]

$$\Delta_{tet} = E_{he} - E_{le} = \frac{\Delta+\delta}{2} - \frac{1}{2}\sqrt{\Delta_{so}^2 - \frac{2}{3}\Delta_{so}\,\delta + \delta^2}. \tag{47}$$

At small δ, i.e., $\delta \ll \Delta$, this is approximately, $\Delta_{tet} \approx \frac{2}{3}\delta$; if the crystal field is positive, the "heavy electron" with $J_z = \pm 3/2$ is shifted upwards in energy with respect to the "light electron" with $J_z = \pm 1/2$. This is shown in Figure 1, panel (a). It is important to recognize that this analysis assumes that the upper $J = 3/2$ conduction band splitting is determined entirely by the interactions among the 6 conduction bands serving as a basis within the model. As described in Ref. 11, calculation of the band structure within DFT shows that this assumption is not valid. The upper $J = 3/2$ conduction band edges, which derive from the R-point of the Brillouin zone in the cubic phase, are close in energy to states derived from the X-point of cubic Brilluoin zone; coupling between the $J = 3/2$ states and the X-derived conduction band states enhances the upper conduction band splitting beyond the result given in Eq. 47, calculated within the 6-band quasi-cubic model outlined here.

B. Orthorhombic distortion

Eq. 41 gives the conduction band edge structure in the presence of simultaneous tetragonal and orthorhombic distortions. A full analytical treatment is complicated by the fact that the energies are cubic functions of the orthorhombic crystal field, ζ, and that the angular momentum about the c-axis is no longer a good quantum number. However, as shown by Fu et al. in Ref. 7, a simple analytical analysis of the effect of the orthorhombic distortion on the lowest conduction band basis functions and energies can be made for the case that the orthorhombic crystal field is small with respect to the spin orbit coupling, $\zeta \ll \Delta_{SO}$. To see this, it is useful to transform Eq. 41 from the total angular momentum basis of Eqs.

39-40 to the basis given in Eq. 44-45 for the tetragonally distorted system. In this case,

$$\hat{H}(\theta,\zeta) = \begin{pmatrix} E_{he} & 0 & \zeta\sin\theta & 0 & 0 & -\zeta\cos\theta \\ 0 & E_{le} & 0 & \zeta\sin\theta & 0 & 0 \\ \zeta\sin\theta & 0 & E_{le} & 0 & 0 & 0 \\ 0 & \zeta\sin\theta & 0 & E_{he} & \zeta\cos\theta & 0 \\ 0 & 0 & 0 & \zeta\cos\theta & E_c & 0 \\ -\zeta\cos\theta & 0 & 0 & 0 & 0 & E_c \end{pmatrix} . \tag{48}$$

In this expression, the energies on the diagonal are given in Eq. 43. Neglecting $\zeta\sin\theta$ in Eq. (48) terms we neglect the coupling induced by the orthorhombic crystal field within the upper conduction band manifold. At the same time we keep the first order corrections to energies and basis functions of the lowest conduction band, resulting in the approximate Hamiltonian,

$$\hat{H}(\theta,\zeta)\approx \begin{pmatrix} E_{he} & 0 & 0 & 0 & 0 & -\zeta\cos\theta \\ 0 & E_{le} & 0 & 0 & 0 & 0 \\ 0 & 0 & E_{le} & 0 & 0 & 0 \\ 0 & 0 & 0 & E_{he} & \zeta\cos\theta & 0 \\ 0 & 0 & 0 & \zeta\cos\theta & E_c & 0 \\ -\zeta\cos\theta & 0 & 0 & 0 & 0 & E_c \end{pmatrix} . \tag{49}$$

In this approximation the energy E_{le} is unchanged, while the lowest conduction band couples with the $J_z = \pm 3/2$ band, E_{he}. The lower coupled branch, which corresponds to the conduction band edge of interest, has energy,

$$E_c(\zeta) \approx \frac{E_c + E_{he}}{2} - \frac{1}{2}\sqrt{(E_{he}-E_c)^2 + 4\zeta^2\cos^2\theta}\ . \tag{50}$$

Figure 2 compares the band edge energy found using approximate Eq. (50) with the energy determined by direct daiagonalizing the full Hamiltonian, Eq.41. Differences in the energy are less than 3 meV up to crystal field values of 500 meV as shown in panel (b) of the figure.

The band edge Bloch function of NCs with orthorhombic crystal structure found in the first order perturbation theory can be written,

$$\begin{aligned} u_{c1}^{orth} &\approx -\cos\phi\sin\theta Z\uparrow + \frac{(\sin\phi - \cos\phi\cos\theta)X - i(\sin\phi + \cos\phi\cos\theta)Y}{\sqrt{2}}\downarrow \\ u_{c2}^{orth} &\approx \frac{(\sin\phi - \cos\phi\cos\theta)X + i(\sin\phi + \cos\phi\cos\theta Y}{\sqrt{2}}\uparrow + \cos\phi\sin\theta Z\downarrow . \end{aligned} \tag{51}$$

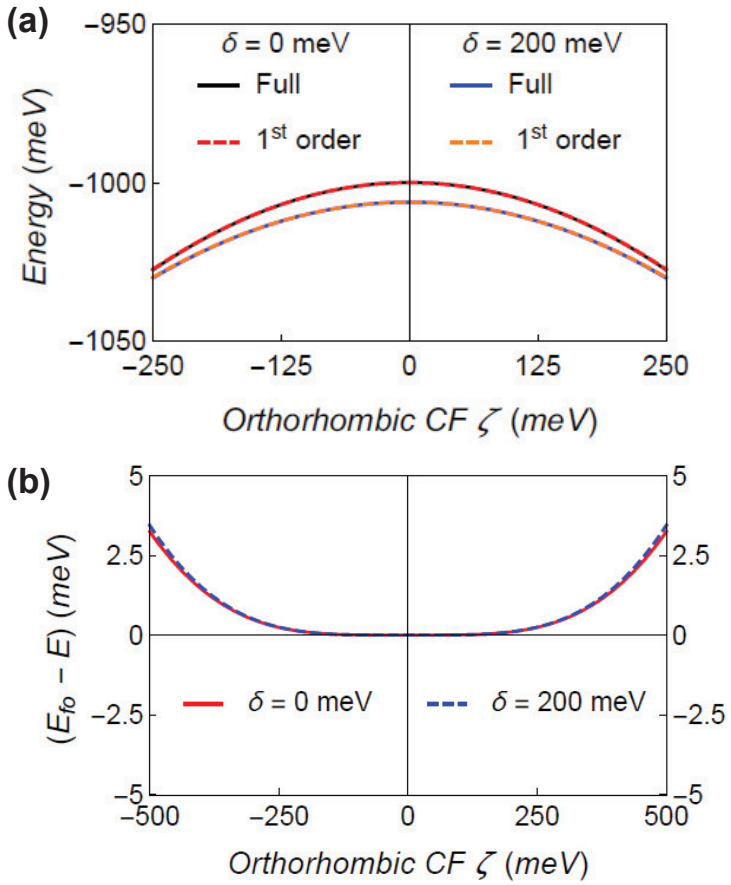

FIG. 2. Comparison of the dependence of the lowest conduction band edge on orthorhombic crystal field ζ calculated by diagonalizing the full Hamiltonian Eq. 41 (solid lines) and in first order perturbation theory using Eq. 50 (dashed lines). Calculations were conducted using spin orbit splitting $\Delta_{SO} = 1.5\,\text{eV}$, for tetragonal crystal field $\delta = 0\,\text{meV}$, shown with black and red dashed lines in panel (a), and $\delta = +200$ meV shown with solid blue and orange dashed lines on panel (a). As in Fig 1 the zero of energy in the plot is the centroid of all six conduction bands (originating from $J = 3/2$ and $J = 1/2$). Panel (b) shows the difference in energy between the solution found in the first order perturbation theory (denoted E_{fo}), versus the energy E found by diagonalization of the full Hamiltonian, Eq. 41. In panel (b) the solid red lines corresponds to $\delta = 0$meV while the blue dashed line corresponds to $\delta = +200$meV.

Here, the phase angle, ϕ, is determined by the spin orbit coupling, Δ_{SO} and the tetragonal and orthorhombic crystal fields, δ and ζ. In the first order perturbation theory ϕ is

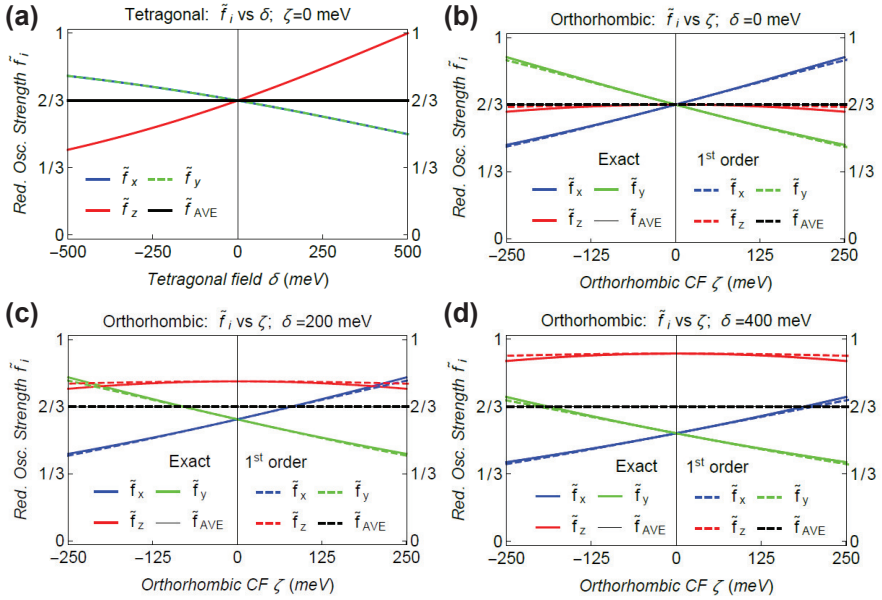

FIG. 3. The dependence of the reduced oscillator transition strengths $\tilde{f}_X$, $\tilde{f}_Y$ and $\tilde{f}_Z$ and their averages for band edge transitions in NCs with tetragonal panel (a), and in NCs with orthorhombic crystal structure, panels (b)-(d), on the crystal field parameters. The oscillator strength is $f_{X_i} = f_0\tilde{f}_{X_i}$ where $f_0 \approx E_p/E_g$ is given in Eq. 54. The spin-orbit coupling in all these plots is taken as $\Delta_{so} = 1.5$eV. The dependences of the oscillator transition strength on δ shown in panel (a) were calculated for $\zeta = 0$. In panels (b), (c) and (d) the oscillator transition strengths is shown as a function of orthorhombic crystal field ζ for zero tetragonal crystal fields $\delta = 0$, (b); $\delta = 200\,\text{meV}$,(c); and $\delta = 400\,\text{meV}$, (d). Solid lines show the results of numerical diagonalization of the "exact" or full Hamiltonian, Eq.41, while dashed lines show the results calculated in the first order perturbation theory using Eq.51. The difference between the first-order result and the result of the full calculation is negligible if $|\zeta| < 100\,\text{meV}$; at $|\zeta| \sim 250\,\text{meV}$ the error in the z-oscillator strength is $< 4\%$. The polarization average in all panels is $2/3$ which is an exact result.

determined as follows:

$$\tan 2\phi = \frac{2\zeta\cos\theta}{E_c - E_{he}} = \frac{-4\zeta\cos\theta}{\Delta_{SO} + \delta + \sqrt{\Delta_{SO}^2 - \frac{2}{3}\Delta_{SO}\delta + \delta^2}}. \tag{52}$$

Equation (52) was derived using the identity,$\tan 2\phi = 2\tan\phi/(1-\tan^2\phi)$, where

$$\tan\phi = \frac{2\zeta\cos\theta}{E_c - E_{he} - \sqrt{(E_c - E_{he})^2 + 4\zeta^2\cos^2\theta}}\,. \tag{53}$$

As noted in the main text, in the case of cubic symmetry, $\delta = 0$, $\zeta = 0$ so that $\tan 2\theta = 2\sqrt{2}$ or $\theta = 35.26^o$ and $\phi = 0$. In that case, the conduction band Bloch functions can be represented as the odd-parity eigenstates of total angular momentum $\boldsymbol{J}$ with $J = 1/2$ and c_1, c_2 revert to the form given in Eq. 39 for perovskite with cubic symmetry. Likewise if $\delta \neq 0$, $\zeta = 0$ these expressions transfer to Eq. 45 for the lowest conduction bands in perovskite tetragonal symmetry of the crystal structure.

To quantify the validity of the approximation culminating in the first order expression for the conduction band-edge Bloch functions, Eq.51, we calculated the transition dipole matrix elements using these expressions and compared them with those calculated using the full Hamiltonian, Eq. 41 or equivalently Eq. 48. In the tetragonal and orthorhombic perovskites, it is clear that the transition dipole matrix elements will be different for the x, y, and z directions. To compare them, it is convenient to calculate the total oscillator strength for the 4 degenerate band-edge transitions, doing so for each x, y, and z polarization components which respectively involve the matrix elements of the $\hat{\boldsymbol{p}}_x$, $\hat{\boldsymbol{p}}_y$, and $\hat{\boldsymbol{p}}_z$ momentum operators. We express these matrix elements via the Kane matrix element, $|P| = |\langle S|\hat{\boldsymbol{p}}_x|X\rangle| = |\langle S|\hat{\boldsymbol{p}}_y|Y\rangle| = |\langle S|\hat{\boldsymbol{p}}_z|Z\rangle|$. Using the definition of oscillator strength for the optical transition between k and m states, $f_{k,m} = 2P_{k,m}^2/(m_0\hbar\omega)$, where $P_{k,m}$ is the matrix element of the momentum operator taken between states k and m, and $\hbar\omega$ is the energy difference between these two states, we can write the oscillator strength for the three band edge transition into $X_i = X, Y, Z$ states with mutually orthogonal dipoles,

$$f_{X_i} = \frac{2P^2}{m_0\hbar\omega}\tilde{f}_{X_i} \equiv f_0\tilde{f}_{X_i} \tag{54}$$

where $f_0 \approx E_p/E_g$ is the magnitude of the oscillator strength, where $E_p = 2P^2/m_0$ is the Kane energy and the energy gap $E_g \approx \hbar\omega$. The reduced oscillator transition strength $\tilde{f}_{X_i} = \tilde{f}_{X_i}(\delta, \zeta)$ contains all of the polarization information and are defined as follows:

$$\tilde{f}_{X_i} = \frac{1}{P^2}\left\{|\langle u_{v1}|\hat{\boldsymbol{p}}_i|u_{c1}\rangle|^2 + |\langle u_{v1}|\hat{\boldsymbol{p}}_i|u_{c2}\rangle|^2 + |\langle u_{v2}|\hat{\boldsymbol{p}}_i|u_{c1}\rangle|^2 + |\langle u_{v2}|\hat{\boldsymbol{p}}_i|u_{c2}\rangle|^2\right\} \ . \tag{55}$$

Using Eq. 38 for the valence band functions u_{v1}, u_{v2} and Eq.51 for the conduction band functions u_{c1}, u_{c2}, the results for the 3 directions are given by,

$$\begin{aligned}
\tilde{f_X} &= (\sin\phi - \cos\theta\cos\phi)^2 \ , \\
\tilde{f_Y} &= (\sin\phi + \cos\theta\cos\phi)^2, \ , \\
\tilde{f_Z} &= 2\cos^2\phi\sin^2\theta \ ,
\end{aligned} \tag{56}$$

resulting in average of the reduced oscillator over the three polarization directions: $\tilde{f}_{ave} = (\tilde{f}_X + \tilde{f}_Y + \tilde{f}_Z)/3 = 2/3$. Importantly, regardless of the crystal field parameters δ and ζ or equivalently the phase angles θ and ϕ, the direction-averaged reduced oscillator strength is conserved and equal to its value in the cubic lattice structure.

While we have shown that $\tilde{f}_{ave} = 2/3$ explicitly using the first-order expressions for the orthorhombic crystal field, the same result can be obtain from the exact solution of Eq. 41. The polarization-average of the reduced oscillator strength is the same whether computed for the $J = 1/2$ lowest conduction band or either of the the upper $J = 3/2$ conduction bands. As a result any admixture between the bands caused by the crystal field splitting preserves the polarization average. Figure 3 shows the reduced oscillator strengths $\tilde{f}_{X_i}$ for X, Y, and Z dipoles as well as their average. Figure 3 shows the result of numerical diagonalization of the full quasi-cubic Hamiltonian, Eq. 41, as well as the results obtained in the first order perturbation theory described by Eq.51. Panel (a) shows the results for the tetragonal phase as a function of tetragonal crystal field δ. The spin-orbit coupling in all these plots is taken as 1.5eV. For the crystal having tetragonal symmetry, $\phi = 0$ and Eq.51 is exact within the limitations of the quasi-cubic model. Panel (b), (c) and (d) show the reduced oscillator strengths calculated for the orthorhombic phase versus orthorhombic crystal field ζ for zero tetragonal crystal field, $\delta = 0$, panel (b); tetragonal crystal field $\delta = 200\,\text{meV}$, panel (c); and tetragonal crystal field $\delta = 400\,\text{meV}$, panel(d). The solid lines in panels (b)-(d) show the exact results while the dashed lines show the results of the first-order perturbation theory. The difference between the latest one and the exact calculation is negligible up to an orthorhombic crystal field of $\sim \pm 100\,\text{meV}$ while the error grows with increasing ζ. The largest error is in the z-polarization term, reaching 3.7% error for orthorhombic crystal field of $|\zeta| \sim 250\,\text{meV}$ with $\delta = 0\,\text{meV}$.

3. DENSITY FUNCTIONAL THEORY CALCULATIONS

Our first-principles calculations of $CsPbBr_3$ and $CsPbI_3$ are based on hybrid density functional theory[12, 13] (DFT) as implemented in the VASP code[14]. These calculations employed projector augmented waves [15] and plane-wave cutoffs of 500 eV, together with spin-orbit coupling (SOC). For the Pb pseudopotentials, semicore $5d$ states were included as valence electrons. k-point meshes of $8 \times 8 \times 8$ were used for the cubic phase, and equivalent

TABLE 1. Calculated normalized lattice parameters (in Å) and direct band gaps (in eV) of $CsPbBr_3$, as determined from hybrid DFT calculations. Experimental lattice parameters from Ref.16 are included in parentheses.

phase	a (Å)	b (Å)	c (Å)	direct band gap (eV)
cubic	–	–	5.95 (5.87)	1.75
tetragonal	–	5.84 (5.84)	6.04 (5.90)	2.18
orthorhombic	5.81 (5.80)	5.87 (5.84)	5.99 (5.88)	2.14

density meshes were employed for the tetragonal phase and orthorhombic phases.

The amount of exact exchange within the hybrid functional was set to 0.35, and a range separation parameter was set to 0.1 $Å^{-1}$ for all calculations. This approach allowed for quantitative accuracy of band structure calculations and momentum matrix elements without excessive computational expense. Perovskite structures for the experimental cubic, tetragonal, and orthorhombic phase of $CsPbBr_3$ were adopted after the experimental measurements in Ref. 16, and all lattice parameters and atomic positions were subsequently relaxed to ensure self-consistency.

These hybrid functional calculations yielded normalized lattice parameters that are in good agreement with experiment (see Table 1) [16]. The minimum direct band gaps calculated for the tetragonal and orthorhombic phases are in good agreement with the 2.2-2.4 eV gaps that have been reported experimentally [16, 17], while the calculated band gap of the cubic phase (1.75 eV) is somewhat smaller.

We also calculated "mimic" $FAPbBr_3$ and $MAPbI_3$ structures, in which the organic cations were replaced by Cs to preserve the inversion symmetry of the experimental structures, an approach taken in Ref. 1 in calculating the properties of tetragonal $MAPbI_3$. The Cs atoms in these structures were explicitly placed at the high-symmetry sites which were nearest to the center of the organic cations. The mimic $FAPbBr_3$ structures consist of $CsPbBr_3$ in a tetragonal structure with lattice constants and Pb and Br ion positions matching the experimental $FAPbBr_3$ $P4/mbm$ structure reported in Ref. 18, and in an orthorhombic structure matching the $Pnma$ structure in Ref. 20. Similarly, the mimic $MAPbI_3$ structures are comprised of $CsPbI_3$ structures with lattice parameters and Pb and I atom positions matching the experimental measurements of Refs. 19 and 21 for the

tetragonal (I4/mcm) and orthorhombic (Pnma) modifications, respectively, again with the replacement of the organic cation by Cs to preserve the inversion symmetry of the experimental structure. For these mimic structures the atomic positions were *not* relaxed prior to calculation of the band structure and band edge wavefunctions.

A. Calculation of short-range exchange

The short-range (SR) exchange interaction can be written as a contact interaction in a form similar to Eq. 29 in the main part of the paper. The exchange Hamiltonian is a matrix operator given by [22, 23]:

$$H^{SR,eh}_{m',n';m,n}(\mathbf{r}_e;\mathbf{r}_h) = +VU_{m',Tn;Tn',m}\delta(\mathbf{r}_e-\mathbf{r}_h) \tag{57}$$

This expression represents the short-range interaction, roughly localized to the unit cell level, between electron-hole pair state m', n' and pair state m, n, where m and n refer respectively to conduction and valance band edge states. Within the formula, $V = N\Omega$ is the crystal volume comprising N unit cells of volume Ω, and T is the time-reversal operator. For direct band gap system with conduction and valence bands m, n, respectively, the exchange matrix element in the expression is given by

$$U_{m',Tn;Tn',m} = \frac{1}{V^2}\int_V d^3r_1 \int_V d^3r_2\ u^*_{m'}(\mathbf{r}_1)[Tu_n(\mathbf{r}_2)]^*U(\mathbf{r}_1,\mathbf{r}_2)Tu_{n'}(\mathbf{r}_1)u_m(\mathbf{r}_2). \tag{58}$$

In the last expression, $U(\mathbf{r}_1,\mathbf{r}_2)$ represents the Coulomb interaction between electrons at positions $\mathbf{r}_1$ and $\mathbf{r}_2$, with account of screening associated with core electrons, and the integrals are taken over the entire crystal volume V. The functions $u_m(\mathbf{r})$ are the band-edge Bloch functions; for a consistent normalization these functions are normalized over the unit cell of volume Ω according to[23]

$$\frac{1}{\Omega}\int_\Omega d^3r\ u^*_m(\mathbf{r})u_m(\mathbf{r}) \equiv 1 \tag{59}$$

Since the exchange interaction, Eq. 57 and the exchange integral in Eq. 58 depend explicitly on the crystal volume V, it is desirable to re-write the exchange interaction in terms of a unit cell exchange constant of the form,

$$H^{SR,eh}_{m',n';m,n}(\mathbf{r}_e;\mathbf{r}_h) = +\Omega U^{cell}_{m',Tn;Tn',m}\delta(\mathbf{r}_e-\mathbf{r}_h). \tag{60}$$

In Eq. 60 then $U^{cell}_{m',Tn;Tn',m} \equiv 1/N\ U_{m',Tn;Tn',m}$, where $N = V/\Omega$ is the number of unit cells in the crystal. To clarify the volume scaling and range of the short-range exchange it is informative to express the Coulomb potential $U(\mathbf{r}_1, \mathbf{r}_2)$ in 58 in terms of its Fourier transform. It has been shown that the dielectric function should be considered as a range-dependent function with the short-range electron-hole exchange interaction being essentially unscreened, while long range interactions are screened by the high frequency dielectric constant [24]. Writing the Coulomb interaction with a short-range dielectric $\epsilon_{SR} \sim 1$ assumed constant,

$$U(\mathbf{r}_1, \mathbf{r}_2) = \frac{e^2}{\epsilon_{SR}|\mathbf{r}_1 - \mathbf{r}_2|} \ = \sum_{\mathbf{q}} U(\mathbf{q}) \ \ e^{i\mathbf{q}\cdot(\mathbf{r}_1 - \mathbf{r}_2)} \tag{61}$$

the Fourier coefficients are given by,

$$U(\mathbf{q}) = \frac{1}{V}\int_V d^3r U(\mathbf{r}) e^{-i\mathbf{q}\cdot\mathbf{r}} = \frac{1}{V}\frac{4\pi e^2}{\epsilon_{SR} q^2} \tag{62}$$

Substituting this into the equation for the unit cell exchange integral, we have,

$$U^{cell}_{m',Tn;Tn',m} = \frac{V}{\Omega}\frac{1}{V^2}\sum_{\mathbf{q}} \frac{4\pi e^2}{V\epsilon_{SR} q^2}\int_V d^3r_1 u^*_{m'}(\mathbf{r}_1) e^{i\mathbf{q}\cdot\mathbf{r}_1} T u_{n'}(\mathbf{r}_1) \int_V d^3r_2 e^{-i\mathbf{q}\cdot\mathbf{r}_2} [T u_n(\mathbf{r}_2)]^* u_m(\mathbf{r}_2) \tag{63}$$

The last equation shows that the exchange integral involves a sum of over the product of the Fourier transforms of the pair Bloch functions Tu_n, u_m. Defining these as follows,

$$A_{Tn,m}(\mathbf{G}) \equiv \frac{1}{V}\int_V d^3\mathbf{r} [T u_n(\mathbf{r})]^* u_m(\mathbf{r}) e^{-i\mathbf{G}\cdot\mathbf{r}}, \tag{64}$$

we note that $A_{Tn,m}(\mathbf{G} = 0) = 0$ because of the orthogonality of the Bloch functions u_m, u_n and we retain only the analytic terms in the sum, by which we mean the terms in the sum with $\mathbf{G} \neq 0$, giving the result [25]:

$$U^{cell}_{m',Tn;Tn',m} = \frac{1}{\Omega}\sum_{\mathbf{G}\neq 0} \frac{4\pi e^2}{\epsilon_{SR} G^2} \left[A_{Tn',m'}(\mathbf{G})\right]^\dagger A_{Tn,m}(\mathbf{G}). \tag{65}$$

Here we have replaced the sum over $\mathbf{q}$ with a sum over reciprocal lattice vectors $\mathbf{G} \neq 0$ reflecting the fact that the functions u_m, u_n are periodic in the lattice. There are in addition non-analytical terms corresponding to $\mathbf{G} = 0$ which comprise the long range exchange[22, 23, 25] which are treated separately following the procedure given in the main text.

It is convenient to write the SR exchange operator in matrix form,

$$\tilde{H}^{SR}(\boldsymbol{r}_e; \boldsymbol{r}_h) = +\Omega\tilde{U}^{cell}\delta(\boldsymbol{r}_e - \boldsymbol{r}_h)\ . \tag{66}$$

where the matrix $\tilde{U}^{cell}$ has matrix elements comprising exchange integrals $U^{cell}_{m',Tn;Tn',m}$ given by Eq. 65 in terms of the Fourier transforms of the pair Bloch functions Tu_n, u_m given in Eq. 64. These can be calculated directly using the Bloch functions from DFT, which were extracted from VASP output using the WaveTrans program.[26] To determine the exchange constant C^{SR}, the resulting matrix $\tilde{U}^{cell}$ is then used in Eq. 66 and the exchange Hamiltonian for the band edge exciton is found by averaging over the exciton wavefunctions, described by Eq. 31 from the main text. The result is,

$$\begin{aligned}\tilde{H}^{SR} &= \tilde{U}^{cell}\Omega \iint_V d^3\mathbf{r}_e d^3\mathbf{r}_h f^*(\mathbf{r}_e,\mathbf{r}_h)\delta(\mathbf{r}_e-\mathbf{r}_h)f(\mathbf{r}_e,\mathbf{r}_h) \\ &= \tilde{U}^{cell}\Omega \int_V d^3\mathbf{r}|f(\mathbf{r},\mathbf{r})|^2 \equiv \tilde{U}^{cell}\Theta \ , \end{aligned} \tag{67}$$

where Θ is the overlap factor developed in the main text in the discussion of the SR exchange interaction. Diagonalizing this matrix we compute the energies of the ground singlet and the upper triplet excitons. We average the difference in energy between the singlet, $U_s\Theta$, and the 3 triplet exciton energies, $U_{t,i}\Theta$ where i runs over the 3 triplet states, to find,

$$\overline{\Delta E^{SR}_{st}} = \overline{\Delta U^{SR}_{st}}\Theta = \left\{ \frac{\sum_{i=1}^{3} U_{t,i}}{3} - U_s \right\} \Theta \ . \tag{68}$$

Since the average singlet-triplet splitting energy is given by the relation, $\overline{\Delta E^{SR}_{st}} = 2/3 C^{SR}\Theta$, which is derived in $\boldsymbol{k}\cdot\boldsymbol{P}$ theory and has been verified using the DFT wavefunctions, the exchange constant C^{SR} is given by,

$$C^{SR} = 3/2 \ \overline{\Delta U^{SR}_{st}} \ . \tag{69}$$

---

[1] Even, J.; Pedesseau, L.; Jancu, J.-M.; and Katan, C., *J. Phys. Chem. Lett.***2013**, 4, 2999 - 3005.

[2] Becker, M. A.; Vaxenburg, R.; Nedelcu, G.; Sercel, P. C.; Shabaev, A.; Mehl, M. J.; Michopoulos, J. G.; Lambrakos, S. G.; Bernstein, N.; Lyons, J. L.; Stiferle, T.; Mahrt, R. F.; Kovalenko, M. V.; Norris, D. J.; Raino, G.; Efros, Al. L. *Nature* **2018**, *553*, 189.

[3] Sercel, P. C.; Lyons, J. L.; Wickramaratne, D.; Vaxenburg, R.; Bernstein, N.; Efros, A. L. Exciton Fine Structure in Perovskite Nanocrystals. Nano Lett. **2019**, *19,* 4068.

[4] Sercel P. C.; Vahala, K. J. *Phys. Rev. B.* **1990**, *42,* 3690.

[5] Kang, I.; and Wise, F.W., *J. Opt. Soc. Am. B* **1997**, *14*, 1632.

[6] Kane, E.O., *J. Phys. Chem. Solids.*, **1957**, *1*, 249.

[7] Fu, M.; Tamarat, P.; Huang,H.; Even, J.; Rogach, A.L.; and Lounis, B., *Nano Lett.* , **2017** *17*, 2895.

[8] Onodera, Y., Toyozawa, Y. *J. Phys. Soc. Jpn.* **1967** *22*, 833.

[9] Nagamune, Y. ; Takeyama, S.; and Miura,N., *Phys. Rev. B* **1991**, *43*, 12401-12405.

[10] Yu, Z. G. *Sci. Rep.*, **2016**, *6*, 28576.

[11] Sercel, P. C.; Lyons, J. L.; Wickramaratne, D.; Vaxenburg, R.; Bernstein, N.; Efros, A. L. Exciton Fine Structure in Perovskite Nanocrystals. Nano Lett. **2019**, *19,* 4068.

[12] Kohn, W.; and Sham, L.J., *Phys. Rev.* **1965**, *140*, A1133.

[13] Heyd, J.; Scuseria, G. E.; and Ernzerhof, M., *J. Chem. Phys.* **2003**, *118*, 8207.

[14] Kresse G.; and Furthmüller, J. *Phys. Rev. B* **1996**, 54, 11169.

[15] Blöchl, P. E. *Phys. Rev. B 50*, 17953.

[16] Stoumpos, C. C.; Malliakas, C. D. ; Peters, J. A.; Liu, Z.; Sebastian, M. ; Im, J. ; Chasapis, T. C.; Wibowo, A. C.; Chung, D. Y.; Freeman, A. J.; Wessels, B. W.; and Kanatzidis, M. G. *Crystal Growth & Design* **2013**, *13*, 2722.

[17] Pazhuk, I. P.; Pydzirailo, N. S.; and Matsko, M. G. *Sov. Phys. Sol. State* **1981**, *23*, 1263.

[18] Shijing Sun, *Synthesis, characterization and properties of hybrid organic-inorganic perovskites for photovoltaic applications*, PhD Thesis, University of Cambridge, 2017.

[19] Frohna K.; Deshpande, T.; Harter, J.; Peng, W.; Barker, B.A.; Neaton, J. B.; Louie, S.G.; Bakr, O. M.; Hsieh, D.; Bernardi, M. *Nature Comm* **2018**, *9*, 1829.

[20] Schueller,E.C.; Laurita,G.; Fabini, D.H.; Stoumpos, C.C.; Kanatzidis, M.G.; and Seshadri, R., *Inorg. Chem.*bf 2018, 57, 695701.

[21] Persson, K., *Materials Data on H6PbCI3N (SG:62) by Materials Project*, **2016**, DOI:10.17188/1317032.

[22] Pikus, G.E.; Bir, G.L. *Zh. Eksp. Teor. Fiz.* **1971**, *60*, 195-208.[*Soviet Physics JETP* **1971** *33* 108].

[23] Bir, G. L. and Pikus, G. E. *Symmetry and strain-induced effects in semiconductors*, Wiley (1974).

[24] Franceschetti, A. ;Wang, L. W. ; Fu,H.; and Zunger,A. *Phys. Rev. B.* **1998**, *58*, R13367.

[25] Rossler, U.; Trebin, H.-R. *Phys. Rev. B* **1981**, *23*, 1961.

[26] Feenstra, R. M.; and Widom, M., *WaveTrans*, https://www.andrew.cmu.edu/user/feenstra/wavetrans/, (Accessed 3 April 2017).